

## Supporting Information

### Evolution of Multivalent Nanoparticle Adhesion via Specific Molecular Interactions

Mingqiu Wang,<sup>1</sup> Shreyas R. Ravindranath,<sup>1</sup> Maha K. Rahim, Elliot L. Botvinick,<sup>1,3,4,5,6</sup> and Jered B. Haun<sup>1,2,4,\*</sup>

<sup>1</sup> Department of Biomedical Engineering, University of California Irvine, Irvine, CA 92697

<sup>2</sup> Department of Chemical Engineering and Materials Science, University of California Irvine, Irvine, CA 92697

<sup>3</sup> Department of Surgery, School of Medicine, University of California Irvine, Irvine, CA 92697

<sup>4</sup> Chao Family Comprehensive Cancer Center, University of California Irvine, Irvine, CA 92697

<sup>5</sup> Beckman Laser Institute, University of California Irvine, Irvine, CA 92697

<sup>6</sup> Edwards Lifesciences Center for Advanced Cardiovascular Technology, University of California Irvine, Irvine, CA 92697

## Table of Contents

Materials and Methods

Results and Discussion

Table S1	Nanoparticle dynamics at low and high antibody density for different $\gamma$ values
Table S2	Final simulation results for the ICAM-1 dimer configuration
Table S3	Final simulation results for the ICAM-1 monomer configuration
Figure S1	Optimizing simulation parameters
Figure S2	Total bond numbers versus time and $\gamma$
Figure S3	Bond biophysics and reaction rates at different $\gamma$ conditions
Figure S4	Bond number dynamics at different $\gamma$ conditions
Figure S5	Corrected bond distributions
Figure S6	Optical tweezers-based dynamic force spectroscopy
Figure S7	Bond numbers for all ICAM-1 configurations
Figure S8	Mean bond potential for dimer and monomer cases
Figure S9	Single bond simulations of nano- and microparticles

## Nanoparticle motion

Nanoparticle movement was governed by the Langevin equations. For nanoparticle translation:

$$\begin{aligned}\frac{d\vec{r}}{dt} &= \vec{v} \\ \frac{d\vec{v}}{dt} &= -\frac{\vec{v}}{\tau_v} + \vec{A} + \vec{K}\end{aligned}\tag{S1}$$

where  $\vec{r}$  is the position vector,  $\vec{v}$  is the velocity vector,  $t$  is time,  $\vec{A}$  is the vector of accelerations resulting from thermal collisions, and  $\vec{K}$  is the vector of accelerations resulting from deterministic forces (bond force, repulsion force, and shear force; see below for detailed descriptions).  $\tau_v$  is the viscous relaxation time, and is given by the Stokes–Einstein relationship for a sphere:

$$\tau_v = \frac{m}{6\pi\mu R}\tag{S2}$$

where  $\mu$  is the solution viscosity,  $R$  is the radius of the nanoparticle, and  $m$  is the mass of the nanoparticle. For the nanoparticle system studied in this work,  $\tau_v = 2.6$  ns. Nanoparticle trajectories were generated by numerically solving Equation S1,<sup>1,2</sup> as follows:

$$\begin{aligned}\vec{r}(t + \Delta t) &= \vec{r}(t) + c_1\vec{v}(t)\Delta t + c_2\vec{K}\Delta t^2 + \partial\vec{r}^G \\ \vec{v}(t + \Delta t) &= c_0\vec{v}(t) + c_1\vec{K}\Delta t + \partial\vec{v}^G \\ c_0 &= \exp(-\Delta t/\tau_v) \\ c_1 &= \frac{(1 - c_0)\tau_v}{\Delta t} \\ c_2 &= \frac{(1 - c_1)\tau_v}{\Delta t}\end{aligned}\tag{S3}$$

where  $\partial\vec{r}^G$  is a random position vector and  $\partial\vec{v}^G$  is a random velocity vector. The elements of these two random vectors were chosen in a position-velocity pairwise fashion from a bivariate Gaussian distribution, which was generated from a SIMD-oriented Fast Mersenne Twister random number generator with seed obtained from system noise. The uniform distribution has a

zero mean, with variances in position ( $\epsilon_r$ ) and velocity ( $\epsilon_v$ ) and correlation coefficient ( $c_{rv}$ ) given by:

$$\begin{aligned}\epsilon_r^2 &= \Delta t \frac{k_B T \tau_v}{m} \left( 2 - \frac{3 - 4 \exp(-\Delta t / \tau_v) + \exp(-2\Delta t / \tau_v)}{\Delta t / \tau_v} \right) \\ \epsilon_v^2 &= \frac{k_B T}{m} (1 - \exp(-2\Delta t / \tau_v)) \\ c_{rv} \epsilon_r \epsilon_v &= \frac{k_B T \tau_v}{m} (1 - \exp(-\Delta t / \tau_v))^2\end{aligned}\tag{S4}$$

Similarly, for nanoparticle rotation:

$$\begin{aligned}\frac{d\vec{\theta}}{dt} &= \vec{\omega} \\ \frac{d\vec{\omega}}{dt} &= -\frac{\vec{\omega}}{\tau_{v,rot}} + \vec{A}_{rot} + \vec{K}_{rot}\end{aligned}\tag{S5}$$

$$\tau_{v,rot} = \frac{I}{27\pi\mu R^3}\tag{S6}$$

where  $\vec{\omega}$  is the vector of angular positions,  $\vec{\theta}$  is the vector of angular velocities,  $\tau_{v,rot}$  is the rotational viscous relaxation time,  $\vec{A}_{rot}$  is the vector of angular accelerations caused by random torques resulting from thermal motion,  $\vec{K}_{rot}$  is the vector of angular accelerations resulting from deterministic torques, and  $I$  is the rotational inertia of the nanoparticle. The expressions in Equation S5 were solved in the same manner as Equation S1, with results analogous to Equation S3. Variances in angular position ( $\epsilon_\omega$ ) and velocity ( $\epsilon_\theta$ ) and correlation coefficient for rotational motion ( $c_{\omega\theta}$ ) are defined identically to Equation S4, but with  $I$  substituted for  $m$  and  $\tau_{v,rot}$  substituted for  $\tau_v$ . For the nanoparticle system studied in this work,  $\tau_{v,rot} = 0.8$  ns. Antibody positions were updated after the nanoparticle was rotated using a three-dimensional rotation matrix.

The translational accelerations ( $\vec{K}$ ) and angular accelerations ( $\vec{K}_{rot}$ ) resulting from deterministic forces are given by

$$\vec{K} = \frac{\sum_b \vec{F}_b + \vec{F}_r + \vec{F}_s}{m} \quad (\text{S7})$$

$$\vec{K}_{rot} = \frac{\vec{T}_s + \sum_b \vec{T}_b}{I} \quad (\text{S8})$$

where  $\sum_b \vec{F}_b$  and  $\sum_b \vec{T}_b$  are vectorial summations of all bond forces and torques, respectively,  $\vec{F}_r$  is the steric repulsion force between the nanoparticle and substrate, and  $\vec{F}_s$  and  $\vec{T}_s$  are the shear force and torque from hydrodynamic flow, respectively.

### Force Calculations

Bond, shear, and steric repulsion forces were treated in a similar manner to previous Adhesive Dynamics and Brownian Adhesion Dynamics works,<sup>3-6</sup>. Bond force was determined by modeling the antibody/ICAM-1 interaction as a Hookean spring (Equation 1). We assumed that molecules were rigidly attached to the surface. Each bond was then described by a time-varying vector  $(\vec{r}_r - \vec{r})$ , from which the force and torque could be calculated as follows:<sup>3</sup>

$$\vec{T}_b = (\vec{r}_r - \vec{r}) \times \vec{F}_b \quad (\text{S9})$$

where  $r$  is the position vector pointing from the center of mass of the nanoparticle.

The nanoparticle and substrate were prevented from coming too close together due to their respective surface protein layers, as well as electrostatic forces and other long-range interactions. These factors result in a net repulsion force that scales with the separation distance. Equation S10 represents the mechanical work that must be performed against nonspecific repulsive forces to bring a unit area of adhesive substrate from an infinite separation distance to a separation distance of  $s$ , as given by Bell:<sup>7</sup>

$$\Gamma(s) = \frac{\xi}{s} \exp\left(-\frac{s}{\tau}\right) \quad (\text{S10})$$

where  $s$  is the separation distance,  $\xi$  is the compressibility coefficient of surface proteins, and  $\tau$  is a measure of the combined thickness of the protein layers. The repulsion force per area is the first order derivative of Equation S10 above, with contact area given by:

$$A = \pi(R^2 - (R + s - \lambda_e)^2) \quad (\text{S11})$$

Therefore the repulsion force was calculated as follows:

$$F_r = \pi\xi(R^2 - (R + s - \lambda_e)^2) \left( \frac{1}{s^2} + \frac{1}{\tau s} \right) \exp\left(-\frac{s}{\tau}\right) \quad (\text{S12})$$

Once separation distance exceeds one bond length, the particle does not experience any repulsion force. As the nanoparticle moves closer to the surface, the repulsion forces increases quickly, acting on the particle uniformly through its center of mass, so as not to generate torque.

Shear force and torque acting on the nanoparticle are modeled using theoretical relationships from Goldman, Cox, and Brenner that are valid near the wall region:<sup>8,9</sup>

$$F_s = 6\pi\mu RSh \left[ 1 + \frac{9}{16} \left( \frac{R}{h} \right) \right] \quad (\text{S13})$$

$$T_s = 4\pi\mu R^3 S \left[ 1 - \frac{3}{16} \left( \frac{R}{h} \right)^3 \right] \quad (\text{S14})$$

where  $h$  is the distance from the particle center to the surface wall and  $S$  is the undisturbed shear rate. These equations are valid for large  $h/R$ . The length of ICAM-1/Ab bond (41.1nm) is relatively large compared to the particle radius (105 nm), and thus  $h/R$  is approximately 1.4. The alternative is the near-wall condition, in which  $h/R$  is approximately 1. However, it should be noted that the difference between these two cases is small, with shear force and torque varying by 20 and 5%, respectively. Since fluid flow was designated along the x-axis,  $F_s$  has a none-zero component in the same direction and  $T_s$  has a none-zero component along the y-axis.

### **Intrinsic rate for bond formation and breakage**

The macroscopic kinetic rates of bond formation ( $k_f^m$ ) and rupture ( $k_r^m$ ) were measured to be  $1.6 \times 10^5 \text{ M}^{-1} \text{ s}^{-1}$  and  $1.1 \times 10^{-4} \text{ s}^{-1}$ , respectively, using surface plasmon resonance experiments.<sup>10</sup> These macroscopic rates were converted to intrinsic rates using the method presented by Bell.<sup>7</sup> First the diffusion-limited rate of formation,  $d_+$ , and dissolution,  $d_-$ , of the encounter complex were calculated as:

$$\begin{aligned} d_+ &= 4\pi D R_{AB} \\ d_- &= 3\pi D / R_{AB}^2 \end{aligned} \quad (\text{S15})$$

where  $D$  is the diffusivity of soluble ICAM-1 and  $R_{AB}$  is the encounter distance for the anti-ICAM-1 antibody and ICAM-1 binding interaction. Using the Stokes-Einstein relation, the diffusion coefficient for soluble ICAM-1 is  $\sim 8.5 \times 10^{-11} \text{ m}^2 \text{ s}^{-1}$ . The value for the encounter distance was assumed to be 0.75 nm, as previously proposed for a hapten-antibody system.<sup>7</sup> The intrinsic bond formation ( $k_f^0$ ) and rupture ( $k_r^0$ ) rates were then found by solving the following system of equations:

$$\begin{aligned} k_f^m &= d_+ k_f^0 / (d_- + k_f^0) \\ k_r^m &= d_- k_r^0 / (d_- + k_f^0) \end{aligned} \quad (\text{S16})$$

The resulting intrinsic rates were  $k_f^0 = 1.6 \times 10^5 \text{ s}^{-1}$  and  $k_r^0 = 1.1 \text{e-4 s}^{-1}$ .

### Measurement of bond mechanical properties using optical tweezers

Biotinylated anti-human ICAM-1 monoclonal antibody (clone BBIG) was purchased from R&D Systems (Minneapolis, MN). Streptavidin-coated, 3  $\mu\text{m}$  polystyrene beads were purchased from Spherotech (Lakeforest, IL). Antibody conjugates were prepared by first washing beads (50  $\mu\text{L}$ ) three times by centrifugation at 1000 x g for 5 minutes and resuspending in 1 mL of PBS containing 1% BSA (PBS+). Beads were then incubated with 5  $\mu\text{g/mL}$  biotinylated antibody for 1 hr at room temperature and washed three 3 times by centrifugation. Normal and ICAM-1 expressing CHO-K1 cells were obtained from ATCC and cultured as recommended. Prior to

experiments, cells were plated on 35 mm x 10 mm cell culture dishes containing glass coverslips on the bottom (MatTek Corporation, Ashland, MA) and cultured overnight. The dishes were then mounted on a motorized piezo-stage with nanometer precision (Physik Instrumente GmbH & Co. KG, Karlsruhe, Germany). All experiments were conducted at 25°C using CO<sub>2</sub> Independent Medium (Thermo Fisher Scientific, Waltham, MA).

Optical tweezers experiments were performed to determine bond rupture force at different force loading rates, similar to previous work using biomembrane force probe and atomic force microscopy.<sup>11–15</sup> Anti-ICAM-1 antibody-coated beads were trapped in a custom-built optical tweezers system described previously.<sup>16,17</sup> A cell was translated using the piezo-stage to the laser-trapped bead, held in contact for a few milliseconds, and then retracted at constant velocity. During each retraction cycle, interactions between the bead and cell resulted in the bead being pulled from the center of the laser trap, which in turn exerted an equal and opposite force on the bead in proportion to the displacement. Thus, bead displacement increased the restoring force of the laser trap until the strength of the interaction was overcome, and then the bead returned to the center of the laser trap. Several hundred contact and release cycles were performed per condition, and bead displacement was tracked using a quadrant photodiode and converted to force based on a calibration of the optical trap, as described.<sup>16,17</sup> Three different retraction velocities of the piezo-stage were tested: 4, 24, and 56  $\mu\text{m/s}$ . These velocities corresponded to loading rates of 213.9, 1544.5, and 2995.8 pN/s, respectively. For each velocity condition, rupture forces measured in each cycle were plotted as normalized histograms, also known as rupture force spectra. Distinct force modes were identified and characterized as arising from non-specific, single bond, or multiple bonding interactions. Finally, single bond rupture force was plotted versus the logarithm of the force loading rate to determine  $\gamma$ , in accordance with the Bell model.<sup>11,15</sup> Control experiments utilized streptavidin-coated beads and normal CHO-K1 cells.



## Results and Discussion

### Simulation optimizations

To ensure accuracy and statistical significance in determining nanoparticle detachment parameters ( $\beta$  and  $k_D^0$ ) based on Equation 8, we tested different nanoparticle ensemble sizes and simulation times. These studies were performed using  $\sigma = 0.1$  N/m,  $\sigma_{ts} = 0.1$  N/m, and  $\gamma = 0.98$  nm at low antibody ( $410 \mu\text{m}^{-2}$ ) and low ICAM-1 ( $21 \mu\text{m}^{-2}$ ) densities. For a 30 s simulation, we found that both  $\beta$  and  $k_D^0$  began to converge around ensemble sizes of 150 nanoparticles (Fig. S1A). Using a 200 nanoparticle ensemble, both  $\beta$  and  $k_D^0$  converged around 20 s (Fig. S1B). Therefore, we selected to use 200 nanoparticle ensembles and 30 s simulation times for all studies. We also tested nanoparticle dynamics at different initial separation distances between the nanoparticle and surface, from 40.3 to 41.9 nm, which was the full range of bond extension or compression lengths allowed while maintaining the bond breakage probability ( $P_r$ , Equation 3) at  $< 10^{-6}$  for this set of conditions ( $\sigma = 0.1$  N/m,  $\sigma_{ts} = 0.1$  N/m, and  $\gamma = 0.98$  nm). We found that nanoparticle detachment dynamics were not significantly affected by initial bond length (Fig. 1C). Finally, we investigated whether new bonds would physically intersect with a current bond before we allowed them to form. We estimated that the diameter of an antibody/ICAM-1 bond was  $\sim 2$  nm. If a potential bond were to form within a distance less than 2 nm from an existing bond, we didn't allow bond formation regardless of the result of the stochastic algorithm. We found this checking for bond intersection reduced mean bond number by 40%, from 3.1 to 2.2, for the set of conditions described above.

### Correction for valency selection to determine mean bond potential

Valency selection is a process by which the detachment of nanoparticles with low bond number potential results in an increase in average bond valency for the remaining population. We desired a method to remove the effect of valency selection so that we could define the true bond steady state and predict the intrinsic bond distribution that was available to each

nanoparticle population. To accomplish this goal, we focused on bond behavior early in the simulation, during the first 0.5 seconds, for the following set of conditions: low antibody density, low ICAM-1 density, and  $\sigma = 0.1$  N/m (Fig. S4). We found that mean bond number remained stable after 0.1 s for low  $\gamma$  values (0.72 to 0.86 nm). At higher  $\gamma$  (0.92 to 1.08 nm), mean bond number increased significantly in the first 0.1 s, but then continued to increase slowly with time in a manner that scaled with the number of detachment events that were concurrently taking place (indicated by red circles at zero bond number). Based on these observations, we postulated that nanoparticles had reached their bond steady state by 0.1 s, and that subsequent increases in mean bond number for the population were the result of valency selection. To test this hypothesis, we assigned a bond potential to each nanoparticle based on the number of bonds at 0.1 s. If the nanoparticle had already detached before 0.1 s, we assigned the maximum bond number that had been attained at any time before detaching, which was usually only one or two bonds. The resulting bond potential histograms are shown in Fig. S5A and B for the low and high antibody conditions, respectively. We also generated bond potential histograms using final bond numbers for nanoparticles that remained bound throughout the simulation or the value seen at 0.1 s prior to detaching (Fig. S5C and D). Distributions using these two methods were very similar, which indicates that the true bond potentials were accurately represented. From these histograms, we can conclude that there was no effect of  $\gamma$  on bond potential. This is consistent with a scenario in which bond potential was only limited by bond availability, likely because formation was highly favorable. As  $\gamma$  increased, bond rupture began to dominate, leading to more dynamic bonding and higher bond numbers being needed to keep nanoparticles bound for at least 30 s. Comparing bond potential distributions in Fig. S5 to final bond distributions at the end of the simulation in Fig. 4, we see that most nanoparticles that detached were only able to form a single bond. Nanoparticles that could form two bonds were very stable at low  $\gamma$ , but began to be lost as  $\gamma$  exceeded 0.92 nm. Only the highest  $\gamma$  values resulted in detachment of nanoparticles with the potential to form three bonds, and

minimal detachment was seen at four bonds and above. Finally, we generated plots of mean bond potential as a function of time, out to 0.5 s (Fig. 4C and D). These were obtained by representing actual bond numbers for bound nanoparticles, or assigning the bond number seen at 0.1 s prior to detachment for those that were lost. The resulting plots clearly demonstrated that bonds did not accumulate with time after reaching the steady state around 0.1 s, and that mean bond potential increased with antibody density from approximately 1.75 to 1.9 (Table S1).

Bond potential histograms and mean bond potential profiles at early time points were similarly determined for the final fitting of experiments using  $\gamma = 0.27$  nm,  $\sigma = 0.8$  N/m, and the various presentations of ICAM-1 including clustered dimers (Fig. 6), dimers, and monomers (Fig. S8).

### **Measuring $\gamma$ using optical tweezers**

Since we could not identify a unique  $\gamma$ - $\sigma$  combination from our mechanical state diagram, but did observe differences in bond biophysical behavior with respect to  $\delta_R$ , we measured the adhesion strength of the antibody/ICAM-1 interaction using optical tweezers-based force spectroscopy. An adherent, live CHO-K1 cell expressing human ICAM-1 was brought into contact with a laser trapped, BBIG antibody coated bead using a motorized piezo-stage with nanometer precision (Fig. S6A). After allowing time for bond formation ( $<0.1$  s), the stage was translated away at a specific velocity to achieve force driven bond dissociation. Bead position was monitored throughout approach and retraction phases (Fig. S6B), and was later converted to force using a calibration of the optical trap. Rupture force histograms obtained at force loading rates of approximately 200, 1500, and 3000 pN/s are shown in Fig. S6C-E. The largest peak in each plot, appearing at low force, corresponded to non-specific interactions (Fig. S6F). Specific antibody/ICAM-1 binding interactions contained additional rupture modes at higher force. Results at 1500 pN/s were easiest to interpret, with only a single high force mode centered at  $17.4 \pm 4.3$  pN that correlated to 17.9% of all interactions. Two high force rupture

modes were observed at the other loading rates. At 200 pN/s, the second rupture mode overlapped significantly with the non-specific mode, while the third mode was very broad and centered over a similar force range seen at 1500 pN/s. We believe that both of these force modes corresponded to specific antibody/ICAM-1 binding, the first under monovalent and the second under multivalent contexts. The monovalent force mode was centered at  $5.0 \pm 2.9$  pN. At 3000 pN/s, we again observed two high force modes. However, in this case we attributed the second mode centered at 28 pN to non-specific interactions because the frequency was far greater than would be expected from a specific binding interaction. Furthermore, it is well known that high force loading rates result in substantially larger standard deviations in rupture force, which is more consistent with the third mode with rupture force centered at  $52.0 \pm 8.9$  pN. Based on these results, we plotted rupture force versus the logarithm of the loading rate (Fig. S6G), and determined that  $\gamma$  was approximately 0.27 nm for our antibody/ICAM-1 interaction based on a linear fit.

**Table S1.** Nanoparticle dynamics at  $\sigma = 0.01$  N/m across different  $\gamma$  values. The conditions highlighted in yellow ( $\gamma = 0.92\text{nm}$ ) best match experimental results in terms of the  $\beta$  and  $k_D^0$  fitting parameters.

Antibody	$\gamma$ (nm)	Bound NP (%)	$\beta$	$k_D^0$ (ms <sup>-1</sup> )	Final Mean Bond Number	Mean Bond Potential
Low Density (410 $\mu\text{m}^{-2}$ )	0.72	72	$0.11 \pm 0.11$	$15 \pm 4$	2.2	1.7
	0.78	64	$0.45 \pm 0.06$	$46 \pm 6$	2.3	1.7
	0.82	62	$0.69 \pm 0.04$	$52 \pm 7$	2.5	1.9
	0.86	54	$0.76 \pm 0.03$	$66 \pm 7$	2.4	1.8
	0.92	37	$0.74 \pm 0.03$	$106 \pm 11$	2.6	1.8
	0.98	18	$0.77 \pm 0.03$	$187 \pm 21$	2.9	1.9
	1.02	4	$0.73 \pm 0.03$	$351 \pm 34$	3.1	1.9
	1.08	2	$0.79 \pm 0.04$	$441 \pm 44$	3.7	2.0
High Density (3400 $\mu\text{m}^{-2}$ )	0.72	93	$0.10 \pm 0.39$	$3 \pm 2$	2.1	1.9
	0.78	89	$0.005 \pm 0.271$	$4 \pm 2$	2.1	1.8
	0.82	82	$0.48 \pm 0.08$	$19 \pm 3$	2.2	1.9
	0.86	73	$0.40 \pm 0.06$	$34 \pm 4$	2.4	1.9
	0.92	66	$0.76 \pm 0.03$	$48 \pm 6$	2.5	1.9
	0.98	48	$0.76 \pm 0.03$	$79 \pm 8$	2.4	1.7
	1.02	39	$0.74 \pm 0.03$	$102 \pm 9$	2.8	1.9
	1.08	14	$0.68 \pm 0.03$	$213 \pm 15$	3.2	2.0

**Table S2.** Final simulation results across all valency conditions for  $\gamma = 0.27$  nm,  $\sigma = 0.8$  N/m, and the dimer configuration for ICAM-1.

ICAM-1 ( $\mu\text{m}^{-2}$ )	Ab ( $\mu\text{m}^{-2}$ )	$\beta$	$k_D^0$ ( $\text{ms}^{-1}$ )	Bound NP (%)	Bond lifetime (s)	$F_{B,R}$ (pN)	Rupture work (pN•nm)	$\delta_R$ (nm)	Final bond number	Bond potential
21	410	$0.75 \pm 0.03$	$100 \pm 10$	52	0.17	307.2	84.2	0.38	2.5	1.4
21	1080	$0.75 \pm 0.03$	$67 \pm 8$	65	0.18	306.2	83.9	0.38	2.4	1.7
21	3400	$0.74 \pm 0.03$	$38 \pm 6$	79	0.18	305.3	83.7	0.38	2.3	2.0
41	410	$0.78 \pm 0.04$	$47 \pm 6$	73	0.08	324.4	88.9	0.41	3.0	2.4
41	1080	$0.81 \pm 0.03$	$30 \pm 4$	83	0.14	316.9	86.8	0.40	2.9	2.6
41	3400	$0.74 \pm 0.06$	$12 \pm 3$	93	0.15	312.7	85.7	0.39	2.9	2.9
134	410	$0.80 \pm 0.90$	$2 \pm 1$	99	0.01	344.1	94.3	0.43	4.7	4.7
134	1080	NA	0	100	0.05	347.0	95.1	0.43	5.0	5.0
134	3400	NA	0	100	0.06	345.0	94.5	0.43	5.1	5.1

**Table S3.** Final simulation results across all valency conditions for  $\gamma = 0.27$  nm,  $\sigma = 0.8$  N/m, and the monomer configuration for ICAM-1.

ICAM-1 ( $\mu\text{m}^{-2}$ )	Ab ( $\mu\text{m}^{-2}$ )	$\beta$	$k_D^0$ ( $\text{ms}^{-1}$ )	Bound NP (%)	Bond lifetime (s)	$F_{B,R}$ (pN)	Rupture work (pN•nm)	$\delta_R$ (nm)	Final bond number	Bond potential
21	410	0.70	65	56	0.13	318.0	87.1	0.40	3.1	2.0
21	1080	0.74	34	73	0.15	313.8	86.0	0.39	3.0	2.4
21	3400	0.68	17	86	0.15	314.6	86.2	0.39	2.9	2.9
41	410	0.62	14	88	0.09	333.1	91.3	0.42	4.0	4.0
41	1080	0.71	3	97	0.09	332.1	91.0	0.42	4.1	4.1
41	3400	NA	0	100	0.09	330.3	90.5	0.41	4.1	4.1
134	410	NA	0	100	0.03	360.0	98.6	0.45	6.2	6.2
134	1080	NA	0	100	0.02	376.0	103.0	0.47	7.2	7.2
134	3400	NA	0	100	0.03	368.0	100.8	0.46	7.1	7.1

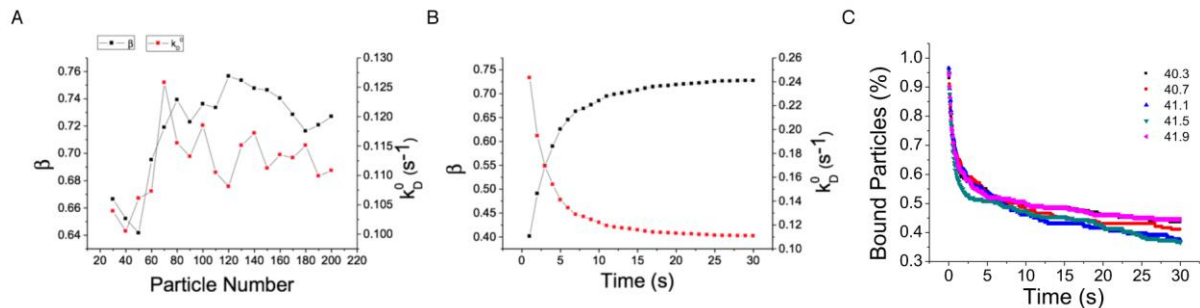


**Figure S1. Optimizing simulations.** (A,B) Nanoparticle detachment profiles were fit using different (A) ensemble numbers and (B) simulation times. Both the  $\beta$  and  $k_D^0$  detachment rate parameters converged for ensembles larger than 150 nanoparticles and simulation times longer than 20 s. (C) Nanoparticle detachment dynamics were unaffected by the initial separation distance between the nanoparticle and surface, within the limits with which a bond would actually form (i.e. conditions with  $P_r < 10^{-6}$ ).



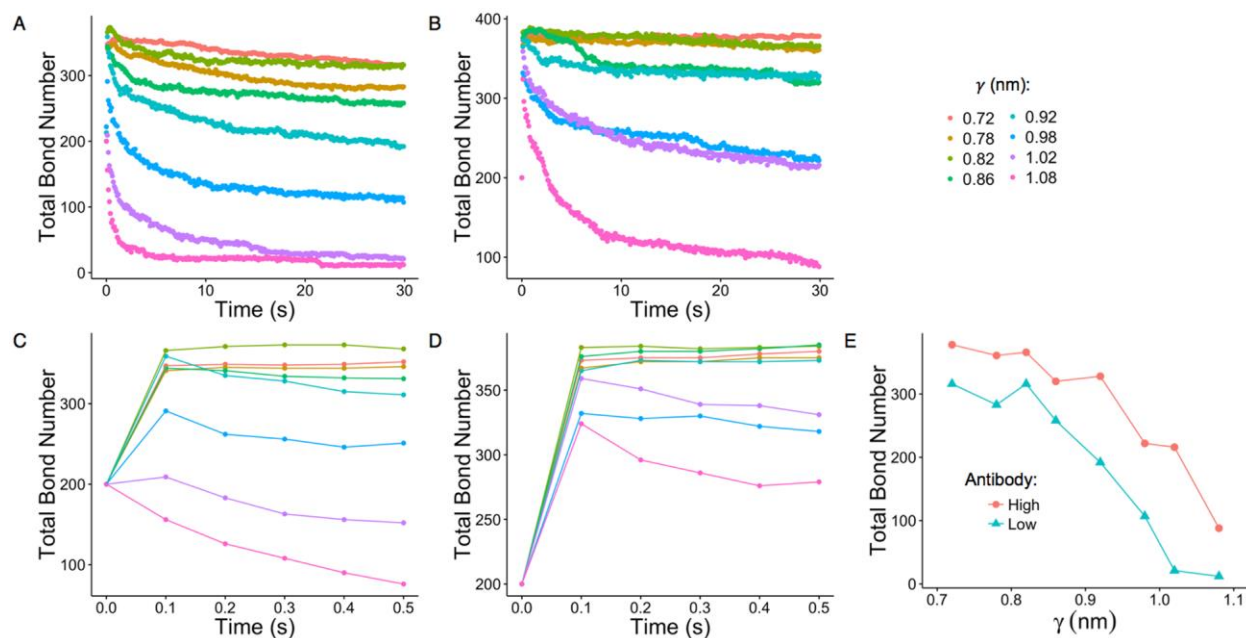


**Figure S2. Total bond numbers versus time and  $\gamma$ .** (A,B) Total bonds across all bound nanoparticles decreased over time for low (A) and high (B) antibody density conditions. Total bonds also decreased at each time point as nanoparticle stability decreased. (C,D) Same data represented only during the first 0.5 s to show that there was an initial increase in bond number that lasted at most 0.1 s, and then decreased with time. (E) Total bond numbers at the end of simulations (30 s) decreased as adhesion became less stable (increasing  $\gamma$ , lower antibody density).

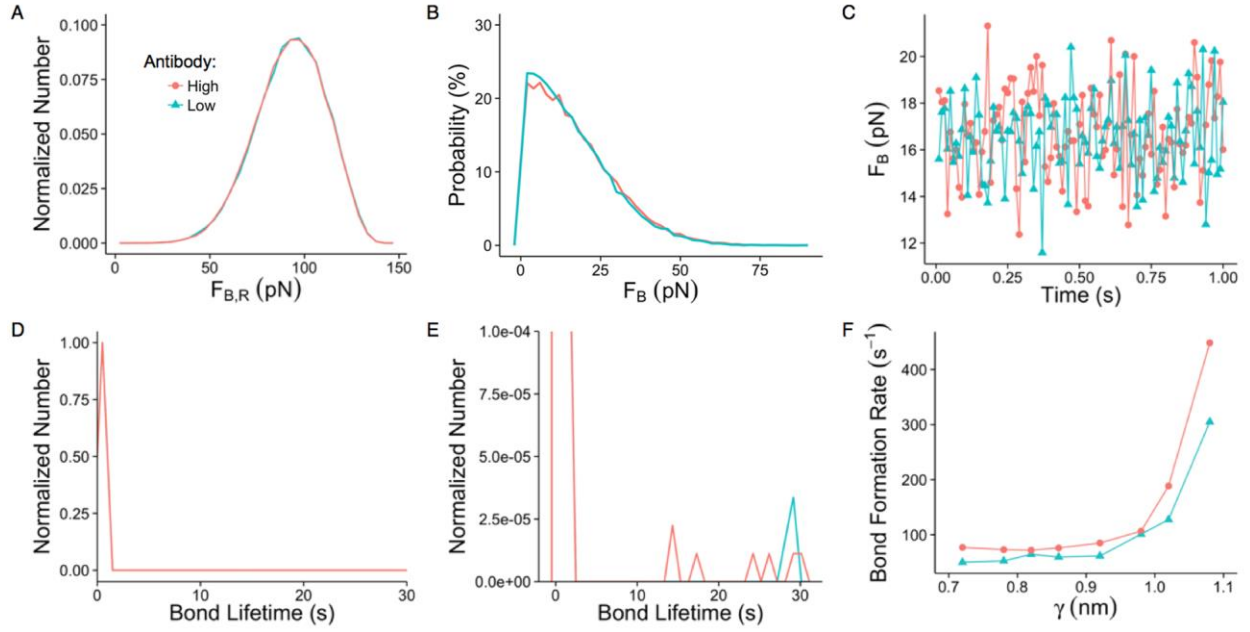


**Figure S3. Bond biophysics and reaction rates.** (A) Bond rupture force ( $F_{B,R}$ ) distributions for  $\gamma = 0.92$  nm for the low and high antibody densities, showing a peak at slightly less than 100 pN. (B) Bond force ( $F_B$ ) distributions for  $\gamma = 0.92$  nm, showing that bonds were typically exposed to forces that were significantly less than  $F_{B,R}$ . (C) Mean  $F_B$  traces at  $\gamma = 0.92$  nm fluctuated around an average value of 16 pN. (D,E) Bond lifetime distributions for  $\gamma = 0.92$  nm, showing that only a few bonds persisted longer than a few seconds. The only difference between panels D and E is the scaling of the y-axis. (F) Bond formation rate, evaluated only within the first 0.1 s of the simulation, was slightly elevated for the high antibody density case.

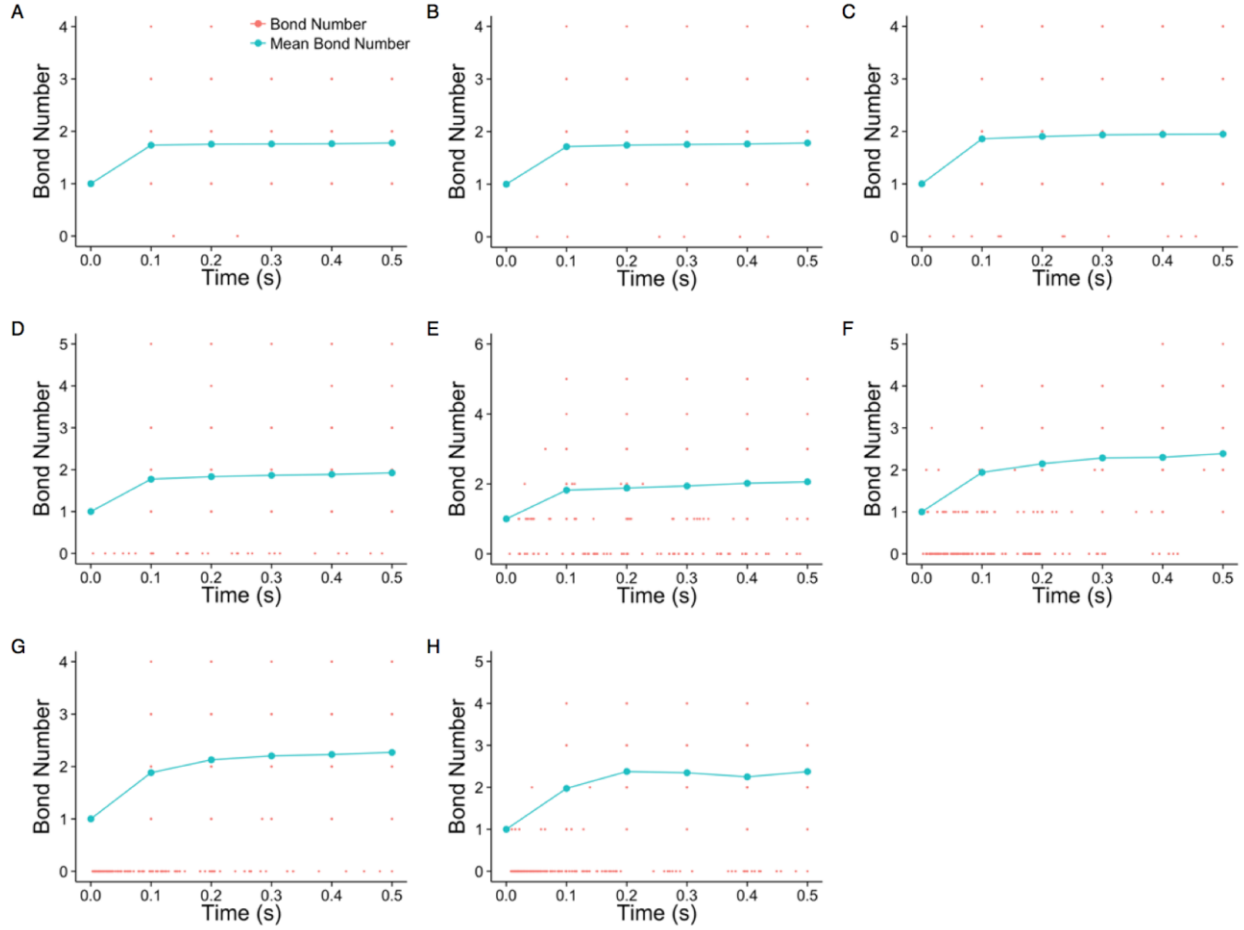


**Figure S4. Bond number dynamics.** Instantaneous and mean bond numbers during the first 0.5 s of the simulation for  $\sigma = 0.1$  N/m, low antibody density, and  $\gamma$  values of (A) 0.72 nm (B) 0.78 nm (C) 0.82 nm (D) 0.86 nm (E) 0.92 nm (F) 0.98 nm (G) 1.02 nm and (H) 1.08 nm. For all conditions, bond number increased predominantly within the first 0.1 s of the simulation, and then continued to slowly increase with time. Detached nanoparticles are indicated by red dots placed at zero bonds. After the 0.1 s time-point, the slow increase in mean bond number correlates with the frequency of detachment events. These results are consistent with the true bond steady state being reached before 0.1 s, and then valency selection leading to the subsequent increases in mean bond number for the remaining population over time.

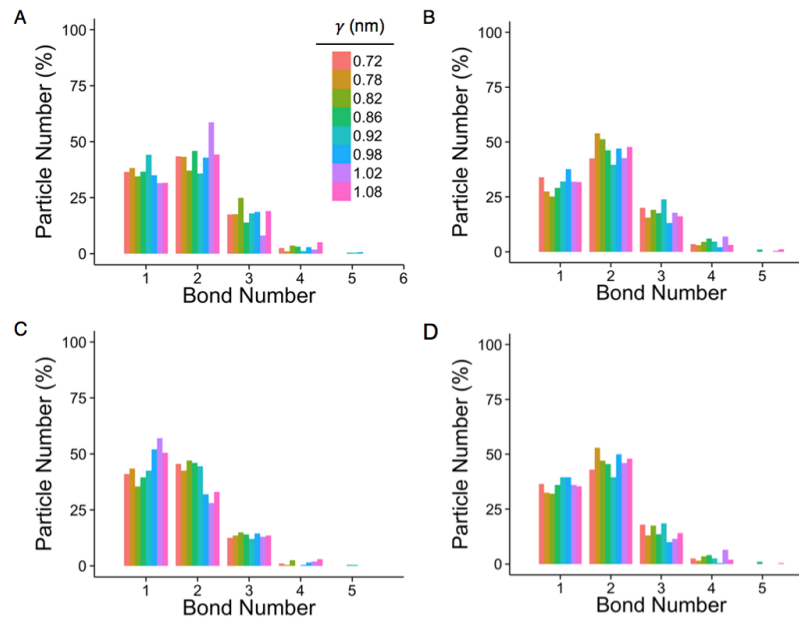


**Figure S5. Corrected bond distributions to reveal bond potential.** (A,B) Bond number histograms were corrected for valency selection using bond numbers seen at the 0.1 s time-point of the simulation for the low (C) and high (D) antibody densities. If a nanoparticle had detached prior to that time point, it was assigned its maximum bond number. (C,D) Bond numbers were corrected for valency selection using either final bond number for nanoparticles that remained bound throughout 30 s simulations or the value noted at 0.1 s prior to detaching for those that were lost. Results are presented at low (A) and high (B) antibody densities. Both correction methods yielded similar results, indicating that the true bond potentials likely had been captured. Bond potential distributions did not vary with  $\gamma$ , but shifted to higher valency with increased antibody density. Note that a significant number of nanoparticles were restricted to a single bond for both cases.

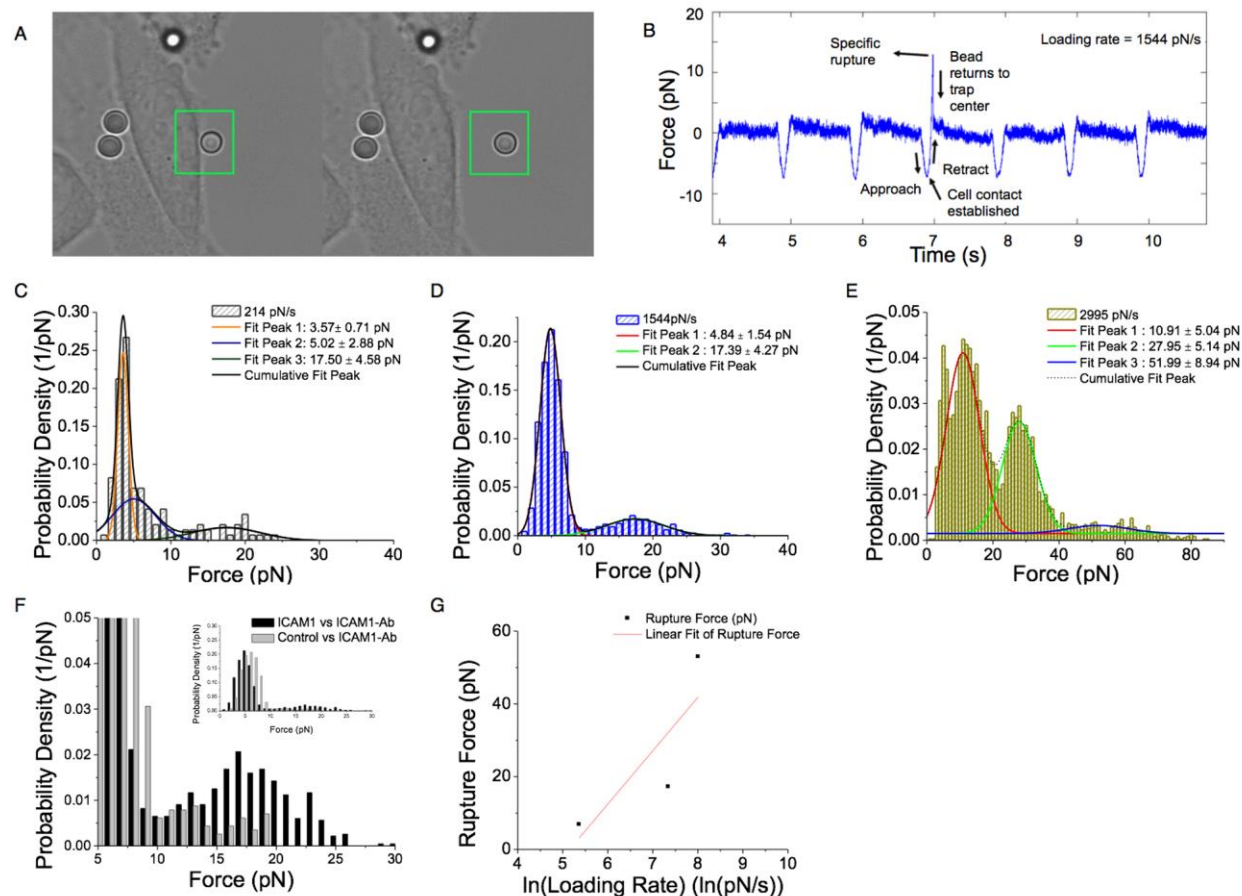


**Figure S6. Dynamic force spectroscopy using optical tweezers.** (A) Micrograph of approach and retraction cycle for an antibody-coated 3  $\mu\text{m}$  bead to an ICAM-1 expressing CHO cell. (B) Continuous force waveform obtained over the course of several approach and retraction cycles during a representative experiment. Each cycle was ~1 s in duration, and peak forces were used to construct rupture force spectra. (C-E) Rupture force spectra at (C) 214, (D) 1544, and (E) 2995 pN/s loading rates. Rupture modes were fit to a Gaussian distribution, and rupture forces are presented as the mean  $\pm$  standard deviation in the legend. (F) Rupture force spectra of specific antibody/ICAM-1 interaction and control interaction at a loading rate of ~1500 pN/s. A specific rupture mode is clearly seen, centered at ~17.5 pN, whereas the control only has a low force mode (<12 pN). Inlay shows the full spectra. (G) Single bond rupture force versus natural logarithm of the loading rate. Red line represents the fit used to determine  $\gamma = 0.27$  nm.

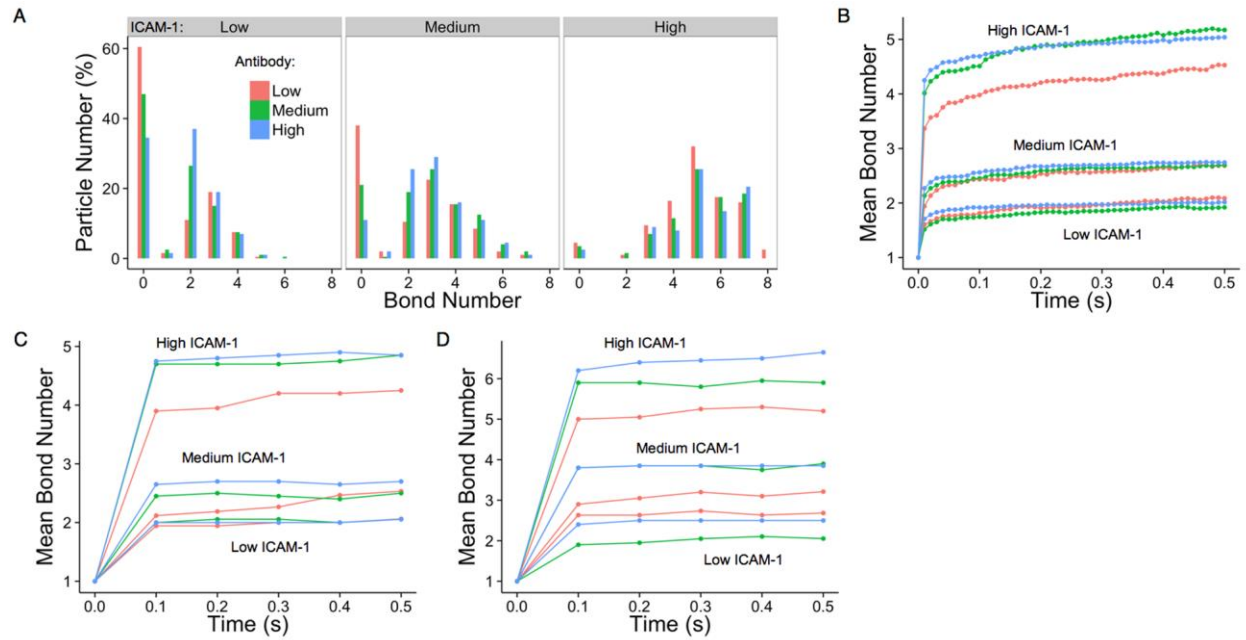


**Figure S7. Bond numbers for all ICAM-1 configurations.** (A) Bond number histograms for ICAM-1 presented as clustered dimers. (B-C) Mean bond number versus time over the first 0.5 s of simulations for ICAM-1 arranged as (B) clustered dimers, (C) dimers, and (D) monomers.

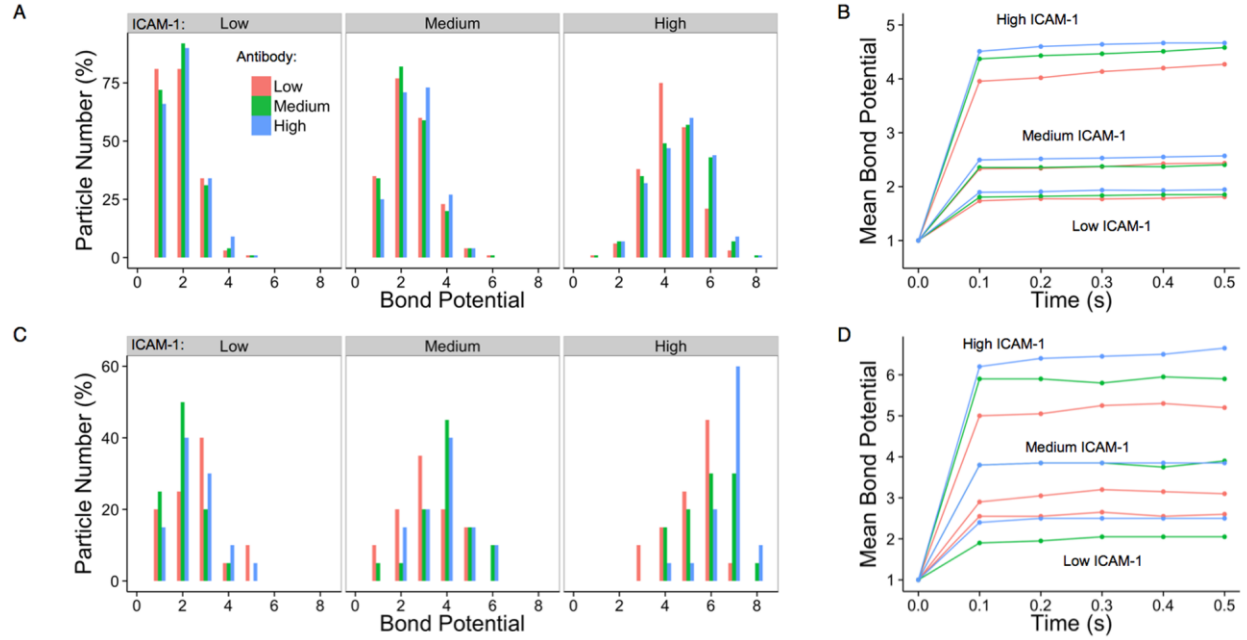


**Figure S8. Mean bond potential for dimer and monomer cases.** (A,C) Bond potential histograms for ICAM-1 arranged as (A) dimers and (C) monomers. (B,D) Traces of mean bond potential for ICAM-1 arranged as (B) dimers and (D) monomers. The bond steady state was attained within 0.1 s at all adhesion molecule densities for both clustering cases.

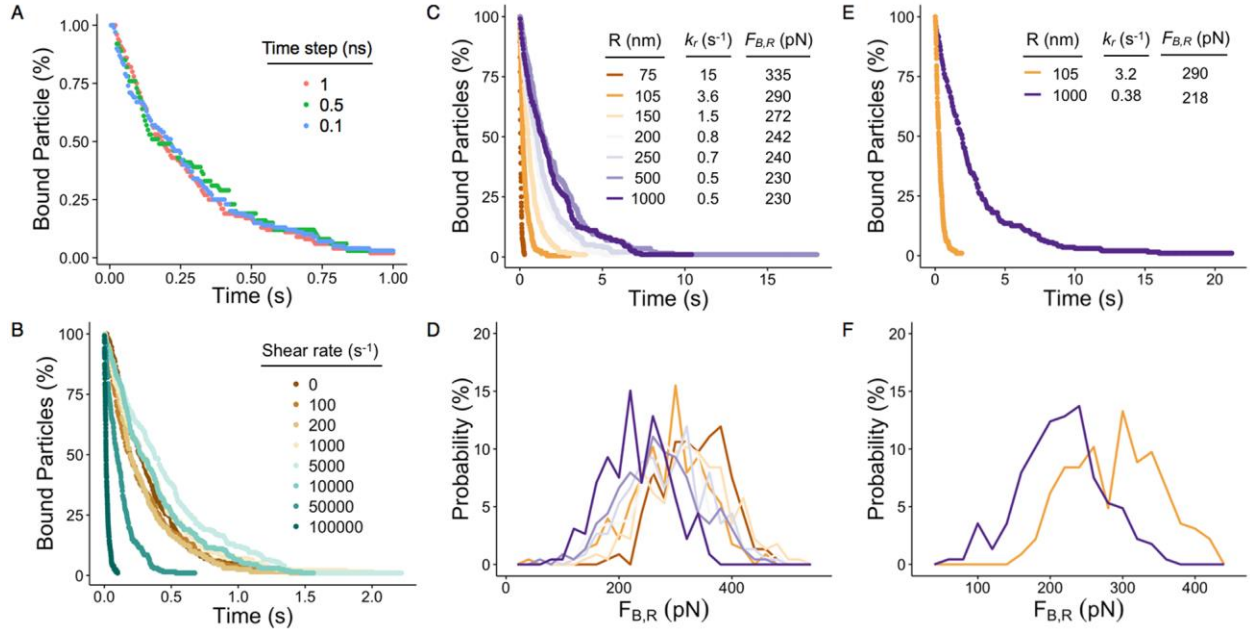


**Figure S9. Single tether simulations.** Nanoparticle detachment was simulated using only a single bond, with no bond formation allowed. (A) Single tether detachment profiles were identical after reducing the simulation time-step from 1 ns down to 0.5 and 0.1 ns. (B) Results were also unchanged when fluid shear flow was removed, as well as when shear rate was increased up to a factor of 100 ( $10,000 s^{-1}$ ). Significant shear force effects were observed starting at  $50,000 s^{-1}$  shear rate, which continued to become stronger at  $100,000 s^{-1}$ . (D-F) Effect of nanoparticle size. (C,D) At  $100 s^{-1}$  shear rate, particle adhesion via a single tether becomes increasingly more stable as radius increases, which can be seen based on (C) delayed detachment profiles and (D) lower bond rupture forces. Inset in (C) displays results from fitting detachment profiles using a single exponential decay to obtain an effective bond detachment rate ( $k_r$ ) and mean  $F_{B,R}$ . No significant difference is observed between particles with 500 and 1000 nm radii, likely due to counter-effects of shear force. (E,F) Without flow, there is minimal change in single tether (E) detachment rate or (F) bond rupture force histogram for a 105 nm radius particle. However, adhesion of a 1000 nm radius particle is considerably more stable than when shear flow is present due to lower forces being experienced at rupture.



## References

- (1) Allen, M. P., and Tildesley, D. J. *Computer simulation of liquids.*; Clarendon Press: **1989**.
- (2) Chandrasekhar, S. Stochastic problems in physics and astronomy. *Rev. Mod. Phys.* **1943**, *15*, 1-89.
- (3) Hammer, D. A., and Apte, S. M. Simulation of cell rolling and adhesion on surfaces in shear flow: general results and analysis of selectin-mediated neutrophil adhesion. *Biophys. J.* **1992**, *63*, 35-57.
- (4) English, T. J., and Hammer, D. A. Brownian adhesive dynamics (BRAD) for simulating the receptor-mediated binding of viruses. *Biophys. J.* **2004**, *86*, 3359-3372.
- (5) English, T. J., and Hammer, D. A. The effect of cellular receptor diffusion on receptor-mediated viral binding using Brownian adhesive dynamics (BRAD) simulations. *Biophys. J.* **2005**, *88*, 1666-1675.
- (6) Trister, A. D., and Hammer, D. A. Role of gp120 trimerization on HIV binding elucidated with Brownian adhesive dynamics. *Biophys. J.* **2008**, *95*, 40-53.
- (7) Bell, G. I. Models for the specific adhesion of cells to cells. *Science* **1978**, *200*, 618-627.
- (8) Goldman, A. J., Cox, R. G., and Brenner, H. Slow viscous motion of a sphere parallel to a plane wall—II Motion through a quiescent fluid. *Chem. Eng. Sci.* **1967**, *22*, 637-651.
- (9) Goldman, A. J., Cox, R. G., and Brenner, H. Slow viscous motion of a sphere parallel to a plane wall—II Couette flow. *Chem. Eng. Sci.* **1967**, *22*, 653-660.
- (10) Eniola, A. O., Willcox, P. J., and Hammer, D. A. Interplay between rolling and firm adhesion elucidated with a cell-free system engineered with two distinct receptor-ligand pairs. *Biophys. J.* **2003**, *85*, 2720-2731.
- (11) Merkel, R., Nassoy, P., Leung, A., Ritchie, K., and Evans, E. Energy landscapes of receptor-ligand bonds explored with dynamic force spectroscopy. *Nature* **1999**, *397*, 50-53.
- (12) Strunz, T., Oroszlan, K., Schäfer, R., and Güntherodt, H. J. Dynamic force spectroscopy of single DNA molecules. *Proc. Natl. Acad. Sci. U. S. A.* **1999**, *96*, 11277-11282.

- (13) Evans, E., Leung, A., Hammer, D., and Simon, S. Chemically distinct transition states govern rapid dissociation of single L-selectin bonds under force. *Proc. Natl. Acad. Sci. U. S. A.* **2001**, 98, 3784-3789.
- (14) Hanley, W., McCarty, O., Jadhav, S., Tseng, Y., Wirtz, D., and Konstantopoulos, K. Single molecule characterization of P-selectin/ligand binding. *J. Biol. Chem.* **2003**, 278, 10556-10561.
- (15) Liu, J., Weller, G. E., Zern, B., Ayyaswamy, P. S., Eckmann, D. M., Muzykantov, V. R., and Radhakrishnan, R. Computational model for nanocarrier binding to endothelium validated using in vivo, in vitro, and atomic force microscopy experiments. *Proc. Natl. Acad. Sci. U. S. A.* **2010**, 107, 16530-16535.
- (16) Shergill, B., Meloty-Kapella, L., Musse, A. A., Weinmaster, G., and Botvinick, E. Optical tweezers studies on Notch: single-molecule interaction strength is independent of ligand endocytosis. *Dev. Cell* **2012**, 22, 1313-1320.
- (17) Kotlarchyk, M. A., Shreim, S. G., Alvarez-Elizondo, M. B., Estrada, L. C., Singh, R., Valdevit, L., Kniazeva, E., Gratton, E., Putnam, A. J., and Botvinick, E. L. Concentration independent modulation of local micromechanics in a fibrin gel. *PLoS One* **2011**, 6, e20201.